Results in Physics 38 (2022) 105627

Contents lists available at ScienceDirect

Results in Physics

journal homepage: www.elsevier.com/locate/rinp

Orbital and equilibrium dynamics of a multiwell potential

H.I. Alrebdi [a], Juan F. Navarro [b,*], Euaggelos E. Zotos [c,d]

[a] Department of Physics, College of Science, Princess Nourah bint Abdulrahman University, P.O. Box 84428, Riyadh 11671, Saudi Arabia
[b] Department of Applied Mathematics, University of Alicante, Carretera San Vicente del Raspeig s/n, 03690, Alicante, Spain
[c] Department of Physics, School of Science, Aristotle University of Thessaloniki, GR-541 24, Thessaloniki, Greece
[d] S.M. Nikolskii Mathematical Institute of the Peoples' Friendship University of Russia (RUDN University), Moscow, 117198, Russia

ARTICLE INFO

Keywords:
Numerical simulations
Hamiltonian systems
Equilibrium points
Escapes

ABSTRACT

We consider a Hamiltonian system associated with the two-well umbilical catastrophe potential D_5, while the corresponding potential contains only one free parameter. We determine how this free parameter affects the equilibrium dynamics of the system by computing their coordinates on the configuration plane, along with their linear stability and type. Additionally, we discuss the influence of the same free parameter on the orbital dynamics of the system by performing a systematic and thorough orbit classification that allows us to reveal the bounded or escaping motion of the test particle.

Introduction

The study of particle's motion in an open Hamiltonian system is a thriving field of research, as confirmed by the number of works carried out on the subject during the last decades (e.g., [1–28]). This importance is due to the fact that the escapes describe a lot of problems in science as, to cite a pair of examples, the decay of metastable states in many fields of physics such as nuclear reactions and or atomic ionization. In this type of system, there exists a value of the energy, E_0, such that if the particle has a value larger than E_0, there is a possibility that it will end leaving the potential well of the system [16]. The previous studies on the escape from a dynamical system have focused primarily on the analysis of the properties of the escape from one-well potentials, with one or more openings through which the particles may escape.

Thus, for instance, Navarro [24] analyzed the dependence of the limiting curves of the basins of escape on the energy in a galactic type Hamiltonian with axial symmetry, which is composed of perturbed harmonic oscillators. The curves of zero velocity of this system present only one exit channel. The escape dynamics of this particular galactic system has been studied previously by Zotos [26] and Navarro [22,23]. Moreover, the escape from multichannel systems have been studied extensively (see e.g., [14,16–21,25,27,28]).

However, far fewer studies have addressed multiwell systems. Multiwell potentials have a highly inhomogeneous phase space. Their main characteristic is that the local minima of the potential are associated with different values of the energy, which leads to mixed states dynamics, that is, a particle with a particular value of the energy shows a different regime of motion depending on if the particle moves in the vicinity of one local minimum or the other.

In a recent paper, [27] (hereafter Paper I), carried out a classification of the types of motion in a Hamiltonian system associated with the two-well umbilical catastrophe potential D_5. In his study, the author performed a numerical exploration of the system to determine the bounded (ordered and chaotic) or escaping nature of the orbits, while also revealing the basins of escape through the different openings of the potential, and also calculating the percentage of escaping orbits and its dependence on the energy of the system.

In this paper, we analyze the same multiwell potential of the lower umbilical catastrophe D_5, in terms of the parameter $\alpha \in [-1, +1]$. In Section "Details of the mathematical model" we give some details about the Hamiltonian and the equations of motion. Section "Equilibrium dynamics" is devoted to the analysis of the equilibria of the system and their local stability. In Section "Orbital dynamics", we investigate the orbital dynamics of the potential. Finally, Section "Concluding remarks" contains the most important conclusions of this work.

Details of the mathematical model

The potential which corresponds to the lower umbilical catastrophe D_5 is given by

$$V(x, y) = \frac{1}{4}x^4 - x^2 + xy^2 + 2\alpha y^2, \tag{1}$$

where α is a free parameter. In our study, we shall consider cases where the numerical value of this parameter lies in the interval $\alpha \in [-1, +1]$.

* Corresponding author.
E-mail addresses: hialrebdi@pnu.edu.sa (H.I. Alrebdi), jf.navarro@ua.es (J.F. Navarro), evzotos@physics.auth.gr (E.E. Zotos).

https://doi.org/10.1016/j.rinp.2022.105627
Received 17 January 2022; Received in revised form 1 May 2022; Accepted 13 May 2022
Available online 24 May 2022

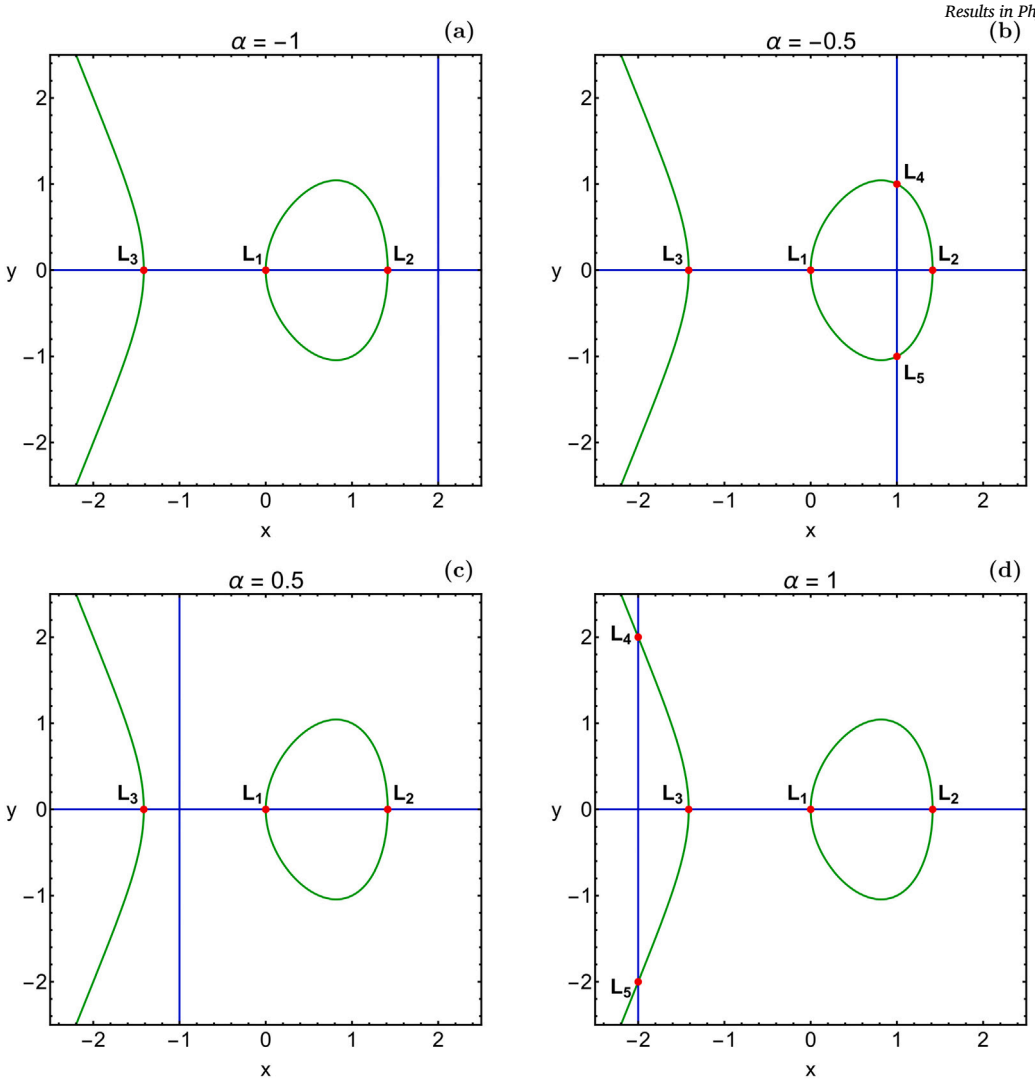

Fig. 1. The geometry of the isoline contours $V_x = 0$ (green) and $V_y = 0$ (red), for characteristic values of the parameter α. The positions of the equilibria are indicated by red dots. (For interpretation of the references to color in this figure legend, the reader is referred to the web version of this article.)

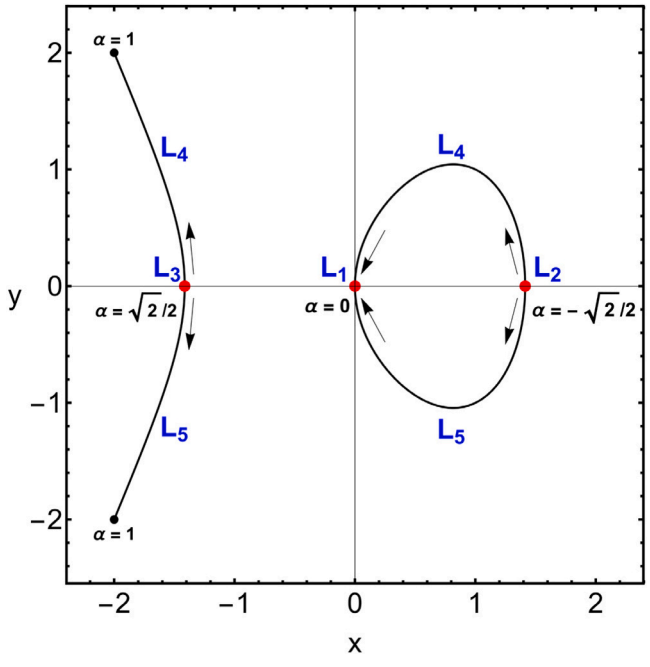

Fig. 2. Parametric evolution of the coordinates on the configuration plane (x, y) of the extra libration points L_4 and L_5, when $\alpha \in [-1, +1]$. The red dots indicate the fixed libration points L_1, L_2, and L_3.

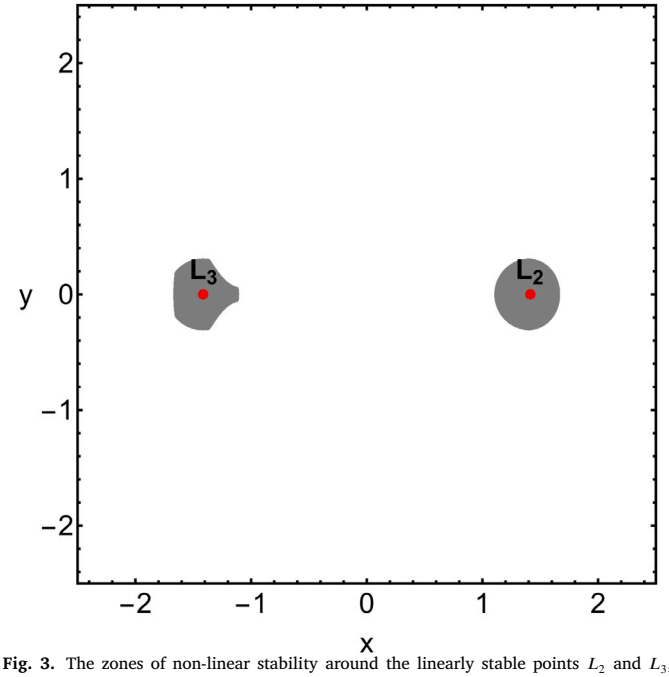

Fig. 3. The zones of non-linear stability around the linearly stable points L_2 and L_3, when $\alpha = 1$.

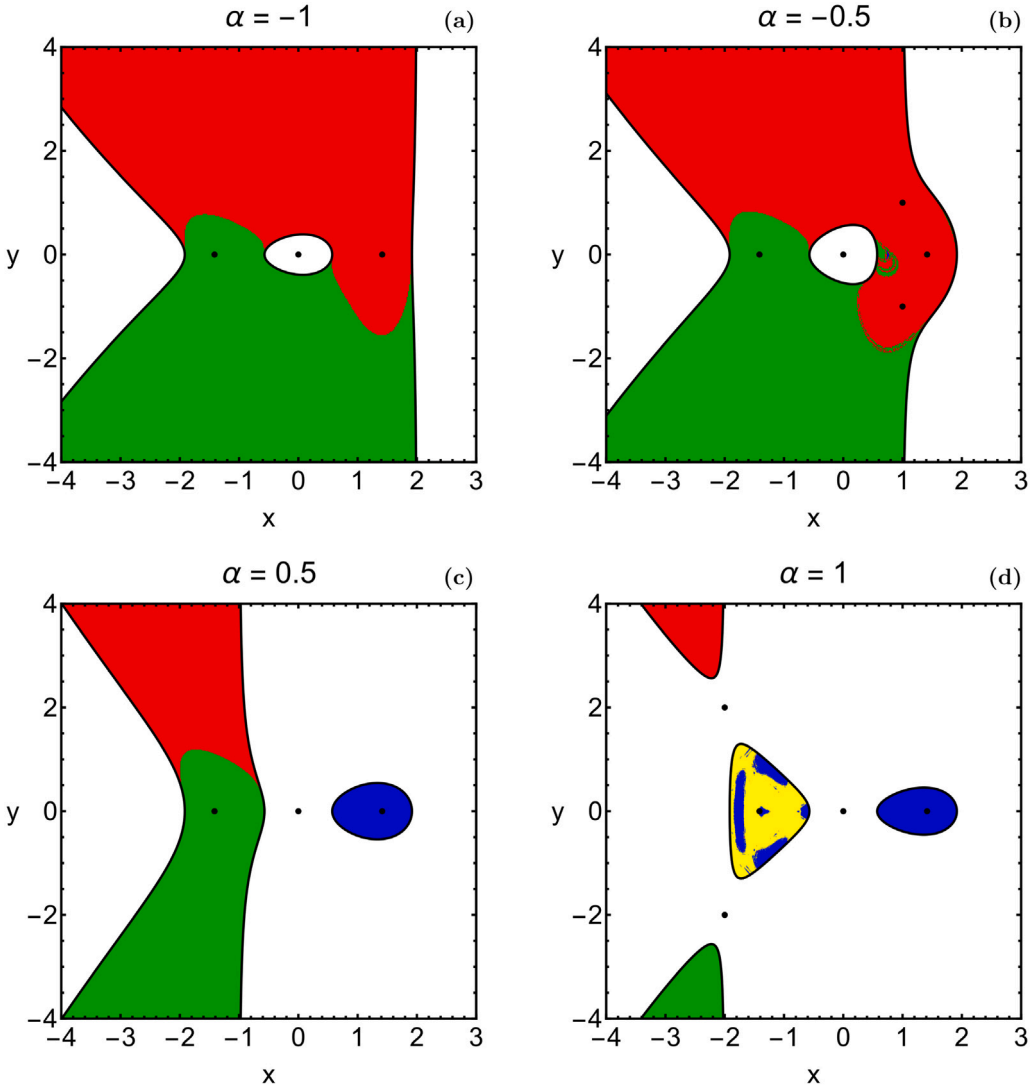

Fig. 4. Basin diagrams revealing the orbit classification on the (x, y) plane, for characteristic values of α, when $E_0 = -0.3$. The correspondence between the character of the trajectories and colors is as follows: chaotic (yellow), sticky (purple), regular (blue), escaping through channel 1 (red), escaping through channel 2 (green). Black dots pinpoint the positions of the system's equilibria. (For interpretation of the references to color in this figure legend, the reader is referred to the web version of this article.)

The set of equations that governs the planar motion of a test particle reads

$$\ddot{x} = -\frac{\partial V}{\partial x} = -V_x(x, y) = -x^3 + 2x - y^2, \tag{2}$$

$$\ddot{y} = -\frac{\partial V}{\partial y} = -V_y(x, y) = -2y\,(x + 2\alpha)\,. \tag{3}$$

The potential's $V(x, y)$ derivatives of second order which are needed for the variational equations as well as for the calculation of the stability of the equilibria, are the following

$$V_{xx}(x, y) = \frac{\partial^2 V}{\partial x^2} = 3x^2 - 2, \tag{4}$$

$$V_{xy}(x, y) = \frac{\partial^2 V}{\partial x \partial y} = 2y, \tag{5}$$

$$V_{yx}(x, y) = \frac{\partial^2 V}{\partial y \partial x} = 2y, \tag{6}$$

$$V_{yy}(x, y) = \frac{\partial^2 V}{\partial y^2} = 2\,(x + 2\alpha)\,. \tag{7}$$

The Hamiltonian of the dynamical system is

$$H = V(x, y) + \frac{1}{2}\left(\dot{x}^2 + \dot{y}^2\right) = E, \tag{8}$$

where E is the test particle's total orbital energy, while it moves inside the regions of the phase space where $V(x, y) \leq E$.

Equilibrium dynamics

The coordinates (x, y) of the equilibrium points of the system on the configuration (x, y) plane are derived by solving the system $V_x(x, y) = V_y(x, y) = 0$. Taking into account the simplicity of these equations, we are able to obtain analytical solutions for the positions of the libration points. In particular, our analysis suggests that the system has always (regardless the value of the parameter α) three collinear equilibrium points located at $(0, 0)$ and $(\pm\sqrt{2}, 0)$. There exist two more equilibria at $(-2\alpha, \pm\sqrt{2\alpha^3 - \alpha})$ which are real only when $-\sqrt{2}/2 < \alpha < 0$ or $\alpha > \sqrt{2}/2$. In fact, the values $\alpha_{c1} = -\sqrt{2}/2$ and $\alpha_{c2} = \sqrt{2}/2$ are critical values of the parameter α.

In order to understand the parametric evolution of the positions of the equilibrium points we show in Fig. 1(a–d) the isoline contours of the curves $V_x = 0$ (green) and $V_y = 0$ (red). The intersections of these curves pinpoint the positions of the libration points (red dots). It is seen that the geometry of the isoline contours $V_x = 0$ is always the same, regardless of the value of α. Specifically, $V_x = 0$ corresponds to a closed elliptical curve between the equilibrium points L_1 and L_2 and

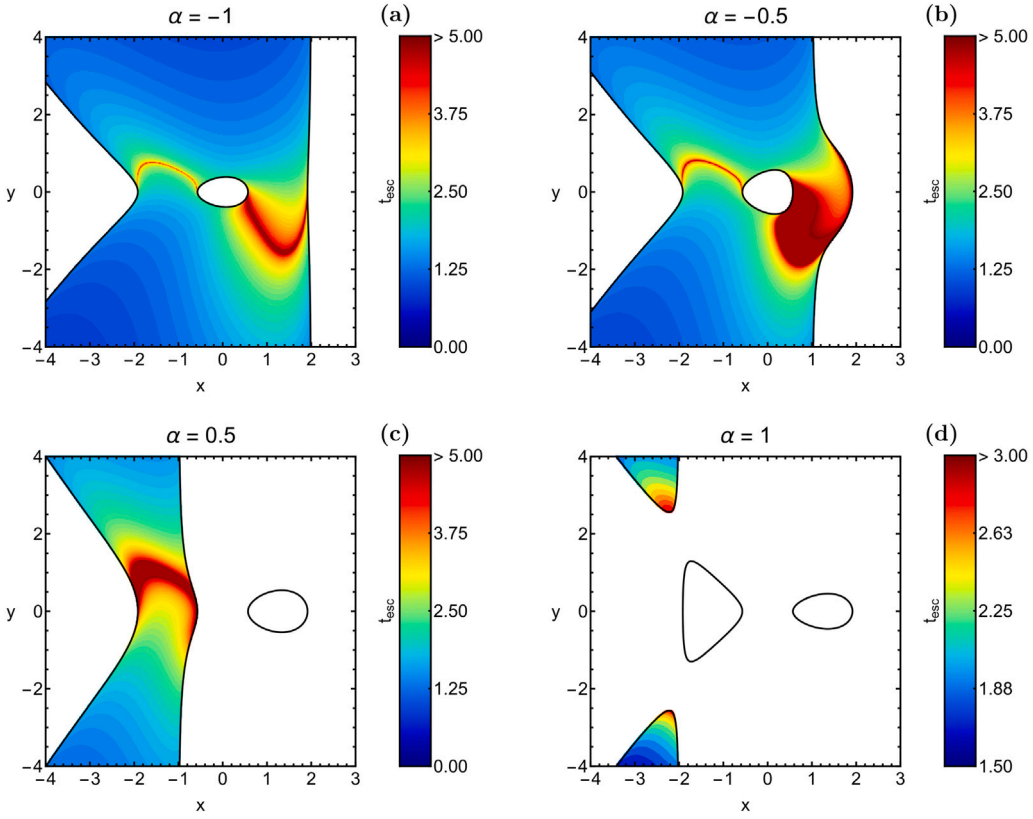

Fig. 5. Distribution of the escape time of the trajectories for the corresponding cases shown in Fig. 4. (For interpretation of the references to color in this figure legend, the reader is referred to the web version of this article.)

a hyperbola where L_3 acts as a vertex. On the other hand, the isoline contours of $V_y = 0$ consist of the horizontal x axis, along with a vertical straight line. This vertical straight line is the only segment that changes position when α varies in $[-1, +1]$. Initially, when $\alpha < \alpha_{c1}$ the vertical line intersects only the horizontal x axis and the system has only three collinear equilibrium points with fixed positions. However, when $\alpha_{c1} < \alpha < 0$, the vertical line intersects the closed elliptical isoline contour $V_x = 0$ and thus two more libration points exist. Then, when $0 < \alpha < \alpha_{c2}$, the vertical line moves between L_1 and L_3 without intersecting any of the $V_x = 0$ segments and therefore we have again the three fixed points of equilibrium. Finally, when $\alpha > \alpha_{c2}$, the moving vertical line intersects the hyperbola $V_x = 0$ which leads to the appearance of two more libration points. In Fig. 2 we present the evolution of the extra equilibria on the plane (x, y), when $\alpha \in [-1, +1]$. We see, that when $\alpha = \alpha_{c1}$, the extra libration points L_4 and L_5 emerge from L_2. As the value of the parameter α increases they move away from L_2 and start approaching L_1. Then, when $\alpha = 0$ they collide with L_1 and they are mutually annihilated. The set of extra libration points appears again when $\alpha = \alpha_{c2}$, where they emerge from L_3. For $\alpha > \alpha_{c2}$ the equilibrium points L_4 and L_5 move away from L_3 and theoretically they tend to infinity as $\alpha \to +\infty$. Comparing the diagrams of Figs. 1 and 2, we see that the evolutionary paths of the extra libration points of the system coincide with the fixed isoline contours of $V_x = 0$.

Knowing the analytical expressions of the coordinates of all the libration points of the system, we can also compute their linear stability. This can be done by linearizing the equations of motion (2) and (3) at any equilibrium point with coordinates (x, y), using the coefficient matrix

$$\mathbf{C} = \begin{pmatrix} 0 & 0 & 1 & 0 \\ 0 & 0 & 0 & 1 \\ -V_{xx} & -V_{xy} & 0 & 0 \\ -V_{yx} & -V_{yy} & 0 & 0 \end{pmatrix}. \tag{9}$$

Then, the linear stability of the equilibria is determined through the roots of the equation $P(\lambda) = 0$, where

$$P(\lambda) = \lambda^4 + \left(V_{xx} + V_{yy}\right)\lambda^2 + V_{xx}V_{yy} - V_{xy}^2, \tag{10}$$

is the characteristic polynomial. In particular, if all four roots of the equation $P(\lambda) = 0$ (evaluated at the libration point (x, y)) are pure imaginary numbers then the corresponding equilibrium point is linearly stable, while in any other scenario the libration point is unstable.

Our computations indicate, that the equilibrium points L_1, L_4, and L_5 are always unstable. On the other hand, the libration point L_2 is unstable when $\alpha < \alpha_{c1}$ and linearly stable when $\alpha > \alpha_{c1}$, while the equilibrium point L_3 is stable only when $\alpha > \alpha_{c2}$.

It is known [29] that around linearly stable points there exist the so-called zones (or regions) of non-linear stability, where a test particle with zero initial velocity remains trapped in the near vicinity of the respective linearly stable equilibrium point, throughout the entire time of the numerical integration. In Fig. 3 we depict the shape of the zones of non-linear stability around the equilibria L_2 and L_3. For the computations we chose the value $\alpha = 1$, where both L_2 and L_3 are linearly stable points. However, additional computations indicated that the shape of these regions remains almost unperturbed for all values of the parameter α, as long as these values correspond to linear libration points.

Finally, we would like to discuss the dynamical nature of the equilibria of the system. The type of a libration point is determined through the number of negative eigenvalues of the matrix

$$\mathbf{M} = \begin{pmatrix} V_{xx} & V_{xy} \\ V_{yx} & V_{yy} \end{pmatrix}. \tag{11}$$

For a system of two degrees of freedom, we have the four cases:

- If there are no eigenvalues with negative real parts, then the corresponding libration point is a minimum of the potential.

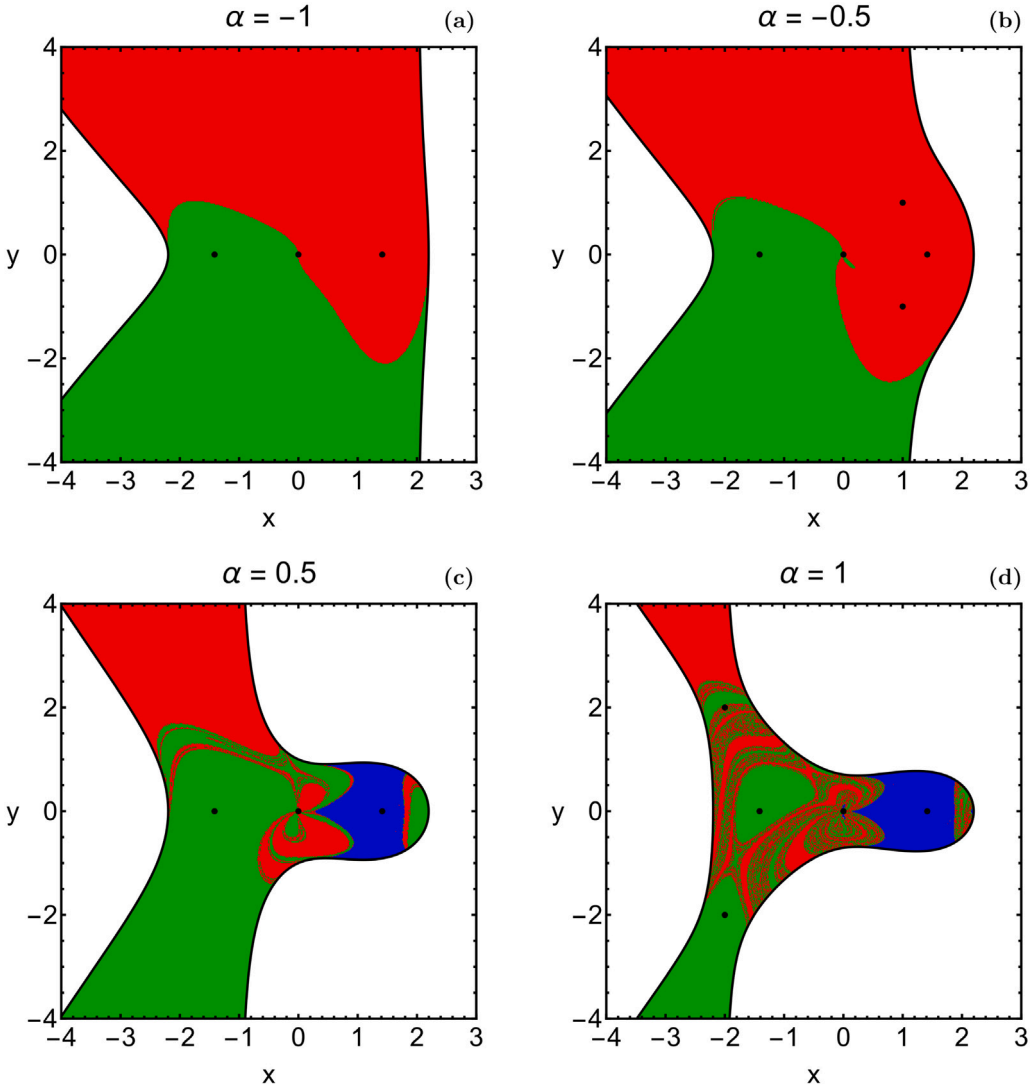

Fig. 6. Basin diagrams revealing the orbit classification on the (x, y) plane, for characteristic values of the parameter α, when $E_0 = 1$. The correspondence between the character of the trajectories and colors is as follows: chaotic (yellow), sticky (purple), regular (blue), escaping through channel 1 (red), escaping through channel 2 (green). Black dots pinpoint the positions of the system's equilibria. (For interpretation of the references to color in this figure legend, the reader is referred to the web version of this article.)

- If there is only one eigenvalue with a negative real part, then the corresponding libration point is an index-1 saddle.
- If there are two eigenvalues with negative real parts, then the corresponding libration point is an index-2 saddle.
- If one or two of the eigenvalues are zero, then we have the case of a degenerate equilibrium point.

For our potential we found that:

- When $\alpha < \alpha_{c1}$, L_1 is in index-2 saddle point, while L_2 and L_3 are index-1 saddles.
- When $\alpha_{c1} < \alpha < 0$, L_1 is an index-2 saddle point, L_2 a minimum of the potential, while L_3, L_4, and L_5 are index-1 saddles.
- When $0 < \alpha < \alpha_{c2}$, L_1 and L_3 are index-1 saddle points, while L_2 is a minimum.
- When $\alpha > \alpha_{c2}$, L_1, L_4, and L_5 are index-1 saddles, while L_2 and L_3 are minima of the effective potential.

Orbital dynamics

In this Section, we investigate the orbital dynamics of the multiwell potential (1). All initial conditions of the orbits are numerically integrated for a total time of 10^4 dimensionless time units. As in Paper I, we apply the geometrical criterion according to which any trajectory is considered to escape if $R = \sqrt{x^2 + y^2} > 10$. Apart from escaping orbits, we have also the case of bounded orbits (those for which $R < 10$, throughout the entire time interval of the numerical integration). In this case, we employ the SALI method [30] for distinguishing between chaotic, sticky, and regular bounded motion.

We begin with the configuration plane (x, y), where all trajectories have initial velocities

$$\dot{x_0} = -\frac{y_0}{r_0}\sqrt{2f_0}, \tag{12}$$

$$\dot{y_0} = \frac{x_0}{r_0}\sqrt{2f_0}, \tag{13}$$

where $r_0 = \sqrt{x_0^2 + y_0^2}$ and $f_0 = 2\left(E_0 - V(x_0, y_0)\right)$.

In Fig. 4(a–d), we present the basin diagrams containing the orbit classification, for $E_0 = -0.3$ and for four characteristic values of the parameter α. In these diagrams, each pixel represents an individual initial condition and it is colored according to the classification of the corresponding trajectory, thus following the graphical approach used in [31,32]. For $\alpha = -1$ (see panel (a)), we see that all the starting conditions lead to escape, through the open zero-velocity curves. In fact, we have two escape channels, the upper one (channel 1) and the

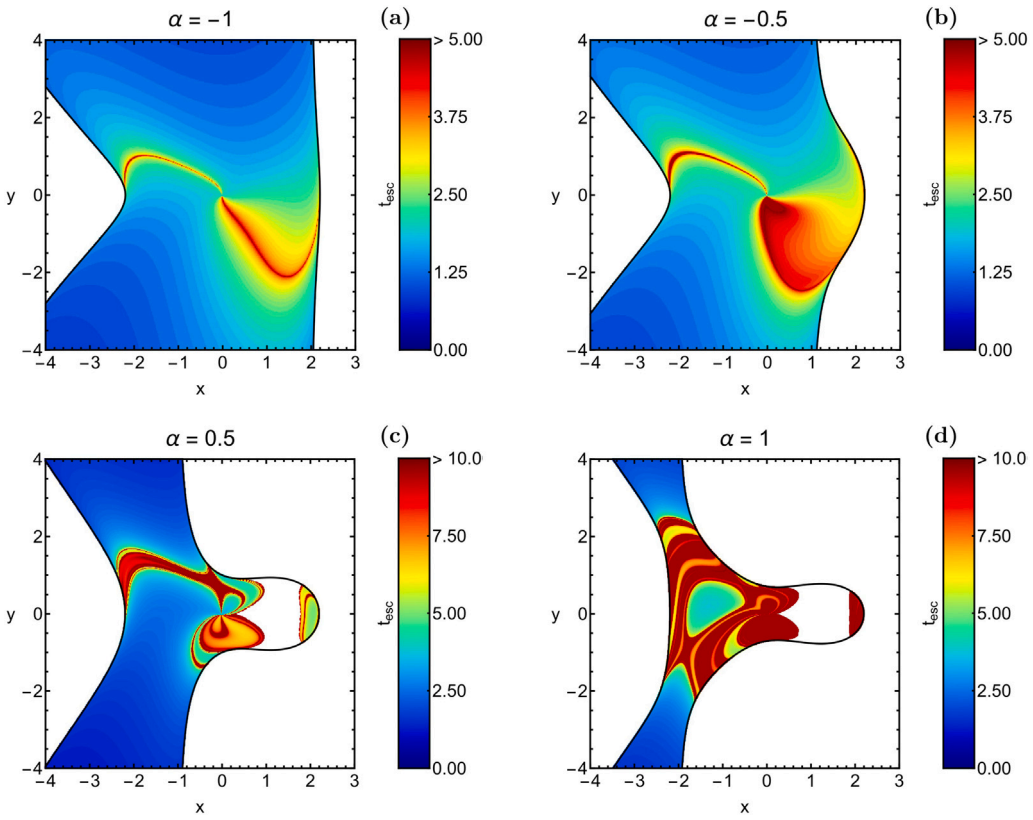

Fig. 7. Distribution of the escape time of the trajectories for the corresponding cases shown in Fig. 6.

lower one (channel 2). It is interesting to note that the basin boundaries are very clear and smooth, without any indication of fractal regions. In panel (b) of Fig. 4, where $\alpha = -0.5$, the overall basin structure remains the same as in panel (a). The only difference is that near the boundaries of the energetically forbidden region around L_1 we see the presence of a complicated structure of escape zones. With a close look, one can observe that at the center of the complicated escape zones lies a tiny island of regular bounded orbits. When $\alpha = 0.5$ (see panel (c)), the zero-velocity curves break and we have two disjoint parts. The part at the left-hand side of the diagram, containing the equilibrium point L_3, is composed entirely of basins of escape. On the other hand, for the second part, at the right-hand side of the diagram (around the libration point L_2), the zero velocity curve is closed, thus containing only bounded regular orbits. When $\alpha = 1$ (see panel (d)), the zero-velocity curves break even further and we have four disjoint parts in total. The two outer parts contain entirely initial conditions of escaping trajectories, while the two parts around the equilibrium points L_2 and L_3 are composed of bounded initial conditions. Interestingly enough, the closed region around L_2 contains entirely regular orbits, while the other closed region around the libration point L_3 contains a mixture of stability islands, as well a unified sea of initial conditions corresponding to sticky and chaotic trajectories.

The color-coded diagrams in Fig. 5(a–d) shows the escape time's t_{esc} distributions of the orbits for the four cases presented in Fig. 4(a–d). As expected, the highest values of the escape time correspond to the boundaries of the basins of escape. In particular, in panel (b) of Fig. 5, we see that the escape time of the trajectories with starting conditions inside the region with the complicated basin structure is considerably higher with respect to the escape time of the orbits with starting conditions outside this region.

The basin diagrams for a positive value of the total orbital energy ($E_0 = 1$) are given in Fig. 6(a–d). When the value of the parameter α is negative ($\alpha = -1$ in panel (a) and $\alpha = -0.5$ in panel (b)) the entire region of energetically allowed motion of the test particle is covered by initial conditions corresponding to escaping trajectories. Once more, as in the case with a negative value of E_0, the basin boundaries are very smooth and clear. This behavior completely changes when the parameter α has positive values, as can be seen in the diagrams of panels (c) and (d), where $\alpha = 0.5$ and $\alpha = 1$, respectively. In both cases, regular bounded motion is possible through a stability island inside the right lobe of the zero velocity curves, around the equilibrium point L_2. Moreover, we can observe the presence of complicated escape basins structures that seem to spiral out from the central libration point L_1 at $(0, 0)$. Our analysis suggests, that the basin structure becomes more complicated as α increases. This will be discussed later by computing the fractal dimension of the phase space, as a function of α.

The corresponding escape time's distributions of the orbits for $E_0 = 1$ are illustrated in the diagrams of Fig. 7(a–d). It becomes evident, that the orbits with starting conditions well inside the basins of escape need no more than 2 time units to cross the escape radius (with velocity pointing outward). On the other hand, trajectories with starting conditions near the boundaries of the escape and regular basins, require more than 5 time units of numerical integration in order to escape. Specifically, in panel (d) of Fig. 7, which corresponds to the case with $\alpha = 1$, we see that for all the starting conditions inside the complicated basin structures the corresponding escape time is of the order of 10 time units, or even higher.

So far, we have presented results on the configuration plane (x, y), for specific values of the total orbital energy E_0. In the diagrams of Fig. 8(a–d) we provide basin diagrams on the (x, E) plane, where for all initial conditions we take $y_0 = \dot{x_0} = 0$. In panel (a), which corresponds to the case with $\alpha = -1$, we see that all the starting conditions lead to escape and in particular, those with $x_0 < 0$ escape through channel 2, while those with $x_0 > 0$ escape through the opposite channel. When the value of the free parameter is $\alpha = -0.5$ (see panel (b)) again the vast majority of the trajectories escape. However, for relatively low values of the total orbital energy and near the right bottom of the potential well there exist a small region of regular bounded orbits.

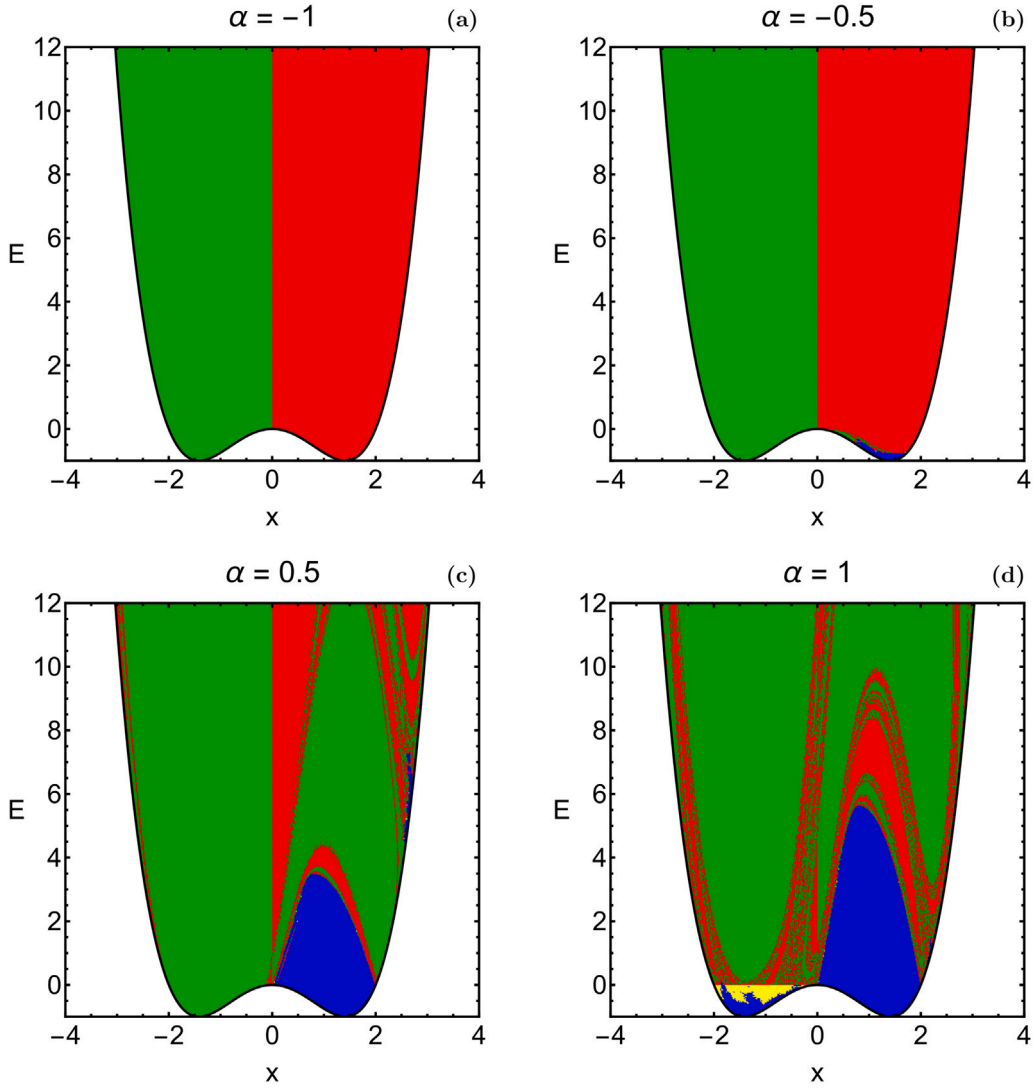

Fig. 8. Basin diagrams revealing the orbit classification on the (x, E) plane, for characteristic values of the parameter α. The correspondence between the character of the trajectories and colors is as follows: chaotic (yellow), sticky (purple), regular (blue), escaping through channel 1 (red), escaping through channel 2 (green). (For interpretation of the references to color in this figure legend, the reader is referred to the web version of this article.)

Our calculations suggest that this region of bounded regular motion grows with increasing value of α. Indeed, in panels (c) and (d) of the same figure which correspond to the cases with $\alpha = 0.5$ and $\alpha = 1$, respectively, we see that the size of the stability region grows inside the right-hand side of the potential well. At the same time, the basin structures, especially on the right-hand side of the basin diagram, become more complicated and interwoven. Furthermore, when $\alpha > \alpha_{c2}$ bounded motion appear also near the left bottom of the potential well. It should be emphasized that the bounded motion that appears on the right-hand side of the potential well corresponds entirely to regular motion, while on the other hand, the bounded motion of the left-hand side of the diagram contains a mixture of all possible types of bounded orbits (mainly regular and chaotic).

In Fig. 9(a–d) we provide the corresponding distributions of the escape time of the orbits with initial conditions on the (x, E) plane. Undoubtedly, the most interesting results are shown in panel (a) of this figure. In panel (a) of Fig. 8, we have seen that all the initial conditions lead to escape, while there is a very clear and smooth transition between the two basins of escape. Moreover, the two basins of escape, corresponding to the two escape channels, are symmetrical with respect to the vertical line $x = 0$. However, in panel (a) of Fig. 9, we see that the distribution of the corresponding $t_{\rm esc}$ of the orbits does not follow the basin structures of Fig. 8. In particular, the distribution is not symmetrical to the $x = 0$ line, while the highest values of $t_{\rm esc}$ are measured near the right bottom of the potential well. Additionally, for all tested values of E, the escape times of the orbits with $x_0 > 0$ are higher with respect to those with $x_0 < 0$. We interpret this behavior as an early indication that bounded motion will emerge at the right-hand side of the basin diagrams for higher values of α. This should be true, taking into account that in panel (b) of Fig. 9 we also observe that around the boundaries of the stability island, located at the right bottom of the potential well, there exist the trajectories with the highest escape times.

The classification of the trajectories on the (x, E) plane indicated that bounded motion is not possible for all values of the parameter α. Additional computations revealed that when $\alpha < \alpha_{c1}$ the entire phase space is completely covered by escaping orbits. Bounded motion, and in particular regular bounded motion, appears at the right-hand side of the potential well, only when $\alpha > \alpha_{c1}$. For positive values of the parameter α, there is no segment of the closed zero velocity curve around L_2. However, regular bounded motion is present, even with open limiting curves.

While presenting the nature of motion on the (x, y) and (x, E) planes we qualitatively discussed the complexity of the phase space.

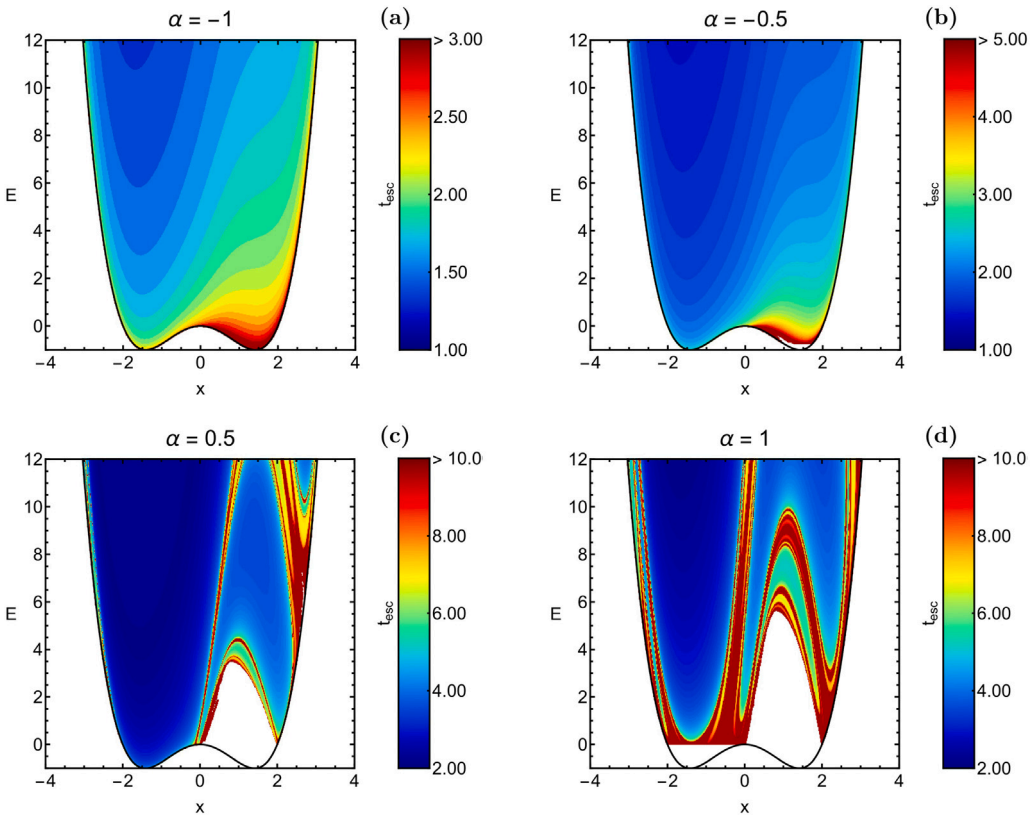

Fig. 9. Distribution of the escape time of the trajectories for the corresponding cases shown in Fig. 8.

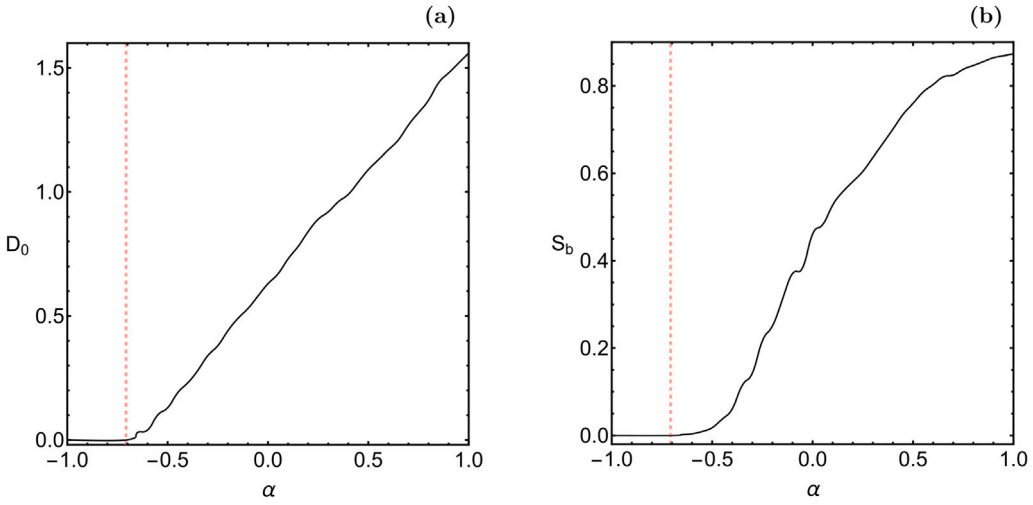

Fig. 10. Parametric evolution of the (a-left): fractal dimension and (b-right): basin entropy of the (x, E) plane, as a function of the parameter α. The vertical, dashed, red line corresponds to the value $\alpha = \alpha_{c1}$.

Nevertheless, a more accurate assessment is required. For this purpose, we computed both the fractal dimension D_0 [33] and the basin entropy S_b [34,35] of the (x, E) plane, as a function of the free parameter α. Our results are shown in Fig. 10(a–b), where we see that the results from two different indicators, regarding the degree of fractality, coincide. In particular, when $\alpha < \alpha_{c1}$ the values of both D_0 and S_b are equal to zero, thus indicating zero fractality. For $\alpha > \alpha_{c1}$ the degree of fractality of the phase space gradually increases which justifies the complex basin structures we observed in the basin diagrams of Figs. 4, 6, and 8. In general terms, we may argue that for negative values of α the basin geometry is relatively simple, while on the other hand for $\alpha > 0$ the basin structures become more complicated, especially due to the addition of the bounded basins to the escape basins of the system.

Concluding remarks

In this article, we worked on the Hamiltonian system associated with the two-well umbilical catastrophe potential D_5. The corresponding two-dimensional potential has only one free parameter which allowed us to fully reveal its properties. Specifically, we explained how the free parameter of the system affects the dynamics of the equilibria by computing their coordinates on the configuration (x, y) plane, along with their linear stability and type (e.g., minimum, index-1

saddle, etc.). Furthermore, we determined the influence of the same free parameter on the orbital dynamics of the system by performing a systematic and thorough orbit classification that allowed us to reveal the test particle's bounded (chaotic, sticky, or regular) and escaping (through channel 1 or 2) motion.

The most important results of our analysis are the following:

1. The dynamical system has either 3 or 5 points of equilibrium, depending on the particular value of the parameter α.
2. Three of the equilibrium points (L_1, L_2, and L_3) are collinear points, on the horizontal x axis, with fixed coordinates.
3. The libration points L_1, L_4, and L_5 are always unstable, while the fixed collinear points L_2 and L_3 can be either linearly stable or unstable, according to the value of the free parameter.
4. Escaping motion is the most dominant type of motion, while the amount of bounded initial conditions grows as the value of α tends to 1.
5. The bounded motion inside the right well of the potential (around L_2) corresponds entirely to regular bounded trajectories. On the other hand, inside the left well of the potential (around L_3) trapped chaotic motion is also possible, especially for energy levels close to $E = 0$.

For the numerical integration of both the equations of motion and the variational equations, we used a double-precision Bulirsch–Stoer routine in FORTRAN 77 [36]. Using an integration time step of the order of 10^{-4} we managed to maintain the conservation of the energy integral (8) with an acceptable numerical error at the order of 10^{-14}.

Declaration of competing interest

The authors declare that they have no known competing financial interests or personal relationships that could have appeared to influence the work reported in this paper.

Data availability statements

The data underlying this article will be shared at a reasonable request to the corresponding author.

Acknowledgments

Our current research project has been funded by Princess Nourah bint Abdulrahman University Researchers, Saudi Arabia Supporting Project number (PNURSP2022R106), Princess Nourah bint Abdulrahman University, Riyadh, Saudi Arabia. The authors would also like to express their warmest thanks to the anonymous referee for the careful reading of the manuscript as well as for all the apt suggestions and comments which allowed us to improve both the quality and the clarity of the paper.

References

[1] Bleher S, Grebogi C, Ott E, Brown R. Fractal boundaries for exit in Hamiltonian dynamics. Phys Rev A 1988;38:930–8.
[2] Blesa F, Seoane JM, Barrio R, Sanjuán MAF. To escape or not to escape, that is the question - perturbing the Hénon-Heiles Hamiltonian. Int J Bifur Chaos 2012;22:1230010-1–9.
[3] Schneider J, Tél T, Neufeld Z. Dynamics of leaking Hamiltonian systems. Phys Rev E 2002;66:066218-1–6.
[4] Seoane JM, Aguirre J, Sanjuán MAF, Lai YC. Basin topology in dissipative chaotic scattering. Chaos 2006;16:023101-1–8.
[5] Seoane JM, Sanjuán MAF, Lai YC. Fractal dimension in dissipative chaotic scattering. Phys Rev E 2007;76:016208-1–6.
[6] Seoane JM, Sanjuán MAF. Exponential decay and scaling laws in noisy chaotic scattering. Phys Lett A 2008;372:110–6.
[7] Seoane JM, Huang L, Sanjuán MAF, Lai YC. Effects of noise on chaotic scattering. Phys Rev E 2009;79:047202-1–4.
[8] Seoane JM, Sanjuán MAF. Escaping dynamics in the presence of dissipation and noisy in scattering systems. Int J Bifur Chaos 2010;9:2783–93.
[9] Siopis CV, Contopoulos G, Kandrup HE. Escape probabilities in a Hamiltonian with two channels of escape. NY Acad Sci Ann 1995;751:205–12.
[10] Siopis CV, Kandrup HE, Contopoulos G, Dvorak R. Universal properties of escape. NY Acad Sci Ann 1995;773:221–30.
[11] Siopis CV, Kandrup HE, Contopoulos G, Dvorak R. Universal properties of escape in dynamical systems. Celestial Mech Dynam Astronom 1996;65:57–681.
[12] Zotos EE. Escapes in Hamiltonian systems with multiple exit channels: Part I. Nonlinear Dynam 2014;78:1389–420.
[13] Zotos EE. Escapes in Hamiltonian systems with multiple exit channels: Part II. Nonlinear Dynam 2015;82:357–98.
[14] Barrio R, Blesa F, Serrano S. Fractal structures in the Hénon–Heiles Hamiltonian. Europhys Lett 2008;82:10003.
[15] Barrio R, Blesa F, Serrano S. Bifurcations and safe regions in open Hamiltonians. New J Phys 2009;11:053004-1–12.
[16] Bolotin YL, Cherkaskiy VA, Ivashkevych GI, Kirdin AL. Over-barrier decay of a mixed state in 2D multiwell potentials. Ukr J Phys 2010;55:838–47.
[17] Contopoulos G. Asymptotic curves and escapes in Hamiltonian systems. Astron Astrophys 1990;231(1):41–5.
[18] Contopoulos G, Kaufmann G. Types of escapes in a simple Hamiltonian system. Astron Astrophys 1992;253(2):379–88.
[19] De Moura APS, Letelier PS. Fractal basins in Hénon–Heiles and other polynomial potentials. Phys Lett A 1999;256:362–8.
[20] Navarro JF. Windows for escaping particles in quartic galactic potentials. Appl Math Comput 2017;303:190–202.
[21] Navarro JF. On the escape from potentials with two exit channels. Sci Rep 2019;9:13174.
[22] Navarro JF. On the integration of an axially symmetric galaxy model. Comput Math Methods 2019;1:e1062.
[23] Navarro JF. Limiting curves in an axially symmetric galaxy. Math Methods Appl Sci 2021;44:993–1002.
[24] Navarro JF. Dependence of the escape from an axially symmetric galaxy on the energy. Sci Rep 2021. (in press).
[25] Navarro JF, Henrard J. Spiral windows for escaping stars. Astron Astrophys 2001;369:1112–21.
[26] Zotos EE. Trapped and escaping orbits in an axially symmetric galactic-type potential. PASA 2012;29:161–73.
[27] Zotos EE. Fractal basin boundaries and escape dynamics in a multiwell potential. Nonlinear Dynam 2016;85:1613–33, (Paper I).
[28] Zotos EE, Cheng W, Navarro JF, Saeed T. A new formulation of the Hénon–Heiles potential with additional singular gravitational terms. Int J Bifurcation Chaos 2020;30:2050197.
[29] McKenzie R, Szebehely V. Non-linear stability around the triangular libration points. Celestial Mech 1981;23:223–9.
[30] Skokos C. Alignment indices: a new, simple method for determining the ordered or chaotic nature of orbits. J Phys A Math Gen 2001;334:10029–43.
[31] Nagler J. Crash test for the Copenhagen problem. Phys Rev E 2004;69:066218.
[32] Nagler J. Crash test for the restricted three-body problem. Phys Rev E 2005;71:026227.
[33] Ott E. Chaos in Dynamical Systems. Cambridge: Cambridge University Press; 1993.
[34] Daza A, Wagemakers A, Georgeot B, Guéry-Odelin D, Sanjuán MAF. Basin entropy: a new tool to analyze uncertainty in dynamical systems. Sci Rep 2016;6:31416.
[35] Daza A, Wagemakers A, Georgeot B, Guéry-Odelin D, Sanjuán MAF. Basin entropy a measure of final state unpredictability and its application to the chaotic scattering of cold atoms. In: Edelman M, et al., editors. Chaotic, Fractional, and Complex Dynamics: New Insights and Perspectives, Understanding Complex Systems. Springer International Publishing AG; 2018.
[36] Press WH, Teukolsky SA, Vetterling WT, Flannery BP. Numerical Recipes in Fortran 90: Numerical Recipes in Fortran 77V. 2. Numerical Recipes in Fortran 90. Cambridge University Press; 1992.